RSC Advances

PAPER

View Article Online
View Journal | View Issue

Cite this: *RSC Adv.*, 2021, **11**, 26607

Ag^0/Au^0 nanocluster loaded Bi_2O_4 photocatalyst for methyl orange dye photodegradation

Najmul Hasan,[a] Daryll J. C. Dalayoan,[a] Jaehyun Lee,[a] Jongmin Lee,[a] Jongseo Kim,[a] Jong-Seong Bae[b] and Chunli Liu *[a]

Received 27th April 2021
Accepted 26th July 2021

DOI: 10.1039/d1ra03278j

rsc.li/rsc-advances

Visible-light-sensitive Ag and Au nanocluster loaded Bi_2O_4 (Ag–Bi_2O_4 and Au–Bi_2O_4) semiconductor photocatalysts have been synthesized. The composite materials exhibited increased photocatalytic degradation of the azo-dye pollutant, Methyl Orange (MO). In addition, Au–Bi_2O_4 (Au-7% wt) showed the highest MO degradation rate (0.05904 min^{-1}) *i.e.* 7.69 times higher than the pristine Bi_2O_4 and 1.4 times higher than 1% Ag–Bi_2O_4. The optical properties of the composites showed that the band gaps of the composite samples 1% Ag–Bi_2O_4 and 7% Au–Bi_2O_4 were 1.96 eV and 2.09 eV, respectively. The increase in the degradation rate is attributed to the decrease of the recombination rate of photoinduced e^-/h^+, caused by the enhanced charge transfer between the metal nanoparticles and Bi_2O_4 as confirmed in the photocurrent measurements. The photocurrent measurements showed increase in the transients output by 8.25 times and 2.75 times for 1% Ag–Bi_2O_4 & 3% Au–Bi_2O_4, respectively as compared to that of the pristine Bi_2O_4. These features further aided the increase in the photocatalytic efficiency while retaining the original physical properties, thus showing the robustness of Bi_2O_4 as a photocatalyst.

1. Introduction

Dyes, in particular azo dyes, are the major by-product of the textile industry. Dyes have been used to color textiles in order to provide a variety of fabrics to choose from, but at the cost of polluting the environment. It has been estimated by the World Health Organization (WHO) that 17–20% of industrial water pollution is caused by the dying treatment of textiles, while about 80% of the dying process is done using azo dyes.[1,2] Azo dyes are known to have acute carcinogenic effects to human and a negative impact on the environment.[3,4] Hence, it is becoming a global urgency to mitigate this issue.

Recently, visible light photocatalysts have been investigated as an alternative to the conventional water processes for dye removal.[5] The photodegradation of dyes require little to no energy other than solar energy to catalyze the pollutant decomposition process. TiO_2 is the most well-known photocatalyst, and has been applied for removal of various dye pollutants.[6–8] However, due to its large band gap (~3.2 eV) it may prove to be ineffective, as most of the UV radiation is blocked by the atmosphere and only 5% is available to be used.[9] Although it has been documented that TiO_2 can be specifically engineered to use as a visible light photocatalyst,[10] the complexity and cost effectiveness has been put into question. Therefore, investigation on alternative visible light photocatalysts with improved properties has been continued.

Recent discoveries of bismuth-based semiconductor photocatalysts have shown promising results in the photodegradation of dyes under visible light. In particular, the Bi_xO_y family of metal oxide semiconductors (Bi_2O_3, BiO_2, BiO_{2-x} or Bi_2O_{4-x}, Bi_2O_4, and Bi_4O_7) have gained much attention. The main features of these materials are their relatively narrow band gap energy, the majority of which are around 1.5–3.0 eV [11] and some of them lie in the visible spectrum, such as Bi_2O_4 (2.0 eV) and Bi_4O_7 (1.89 eV). These materials have absorbance spectra mostly in the range of 600–700 nm and exhibit high photocatalytic activation efficiency. The visible light sensitivity of these materials can be attributed to the co-existence of the bivalent Bi(III) and Bi(V) ions.[12–14] Due to the mentioned features, several visible light responsive Bi-based photocatalyst materials have been reported for the successful degradation of pollutants. For example, the *Z*-scheme MoO_3/Bi_2O_4 composite synthesized by a hydrothermal method showed approximately 2 times enhanced photocatalytic efficiency.[15] Similarly, magnetic quantum dots modified *Z*-scheme Bi_2O_4/g-C_3N_4 has been reported to have superior hydroxyl radical productivity for the degradation of rhodamine B.[16] A type II heterojunction Bi_2O_4/TiO_2 with enlarged interfacial contract areas has been developed using flower-like hierarchical TiO_2 sphere with rich mesopores and macropores for the degradation of MO.[17] Dai *et al.* reported the enhanced interfacial charge transfer (IFCT) for Fe(III) modified Bi_2O_4 nano-rods.[18] They reported an enhanced photocatalytic activity by h^+ and $^{\bullet}O_2^-$ as major reactive species

[a]*Department of Physics and Oxide Research Center, Hankuk University of Foreign Studies, Yongin, 17035, Republic of Korea. E-mail: chunliliu@hufs.ac.kr*
[b]*Busan Center, Korea Basic Science Institute, Busan, 46742, Republic of Korea*

taking part in the photodegradation of water pollutants. In addition, some other Bi based photocatalysts used for degradation of organic pollutants such as AgI/$BiSbO_4$ heterojunctions,[19] Bi_2WO_4,[20] and $BiSbO_4$/BiOBr nanoarchitecture[21] have been reported. The $BiSbO_4$/BiOBr nanoarchitecture showed efficient visible-light driven photocatalytic performance due to increased separation and transfer of photogenerated carriers and generation of $^{\bullet}O_2^-$ as the major reactive species.

Bi_2O_4 in particular has been well documented to have good azo dye degradation properties. Owing to its narrow band gap and band positions, *i.e.* −0.37 V *vs.* NHE for conduction band and +1.63 V *vs.* NHE for its valence band,[14] it is capable of producing reactive species such as the superoxide and hydroxyl radical species ($O_2^{-\bullet}$ and $^{\bullet}OH$) that can degrade azo dyes. In addition, it is relatively simple to synthesize Bi_2O_4 using the hydrothermal method from the prerequisite $NaBiO_3$. Furthermore, Bi_2O_4 is relatively stable in the photocatalysis process and is highly reusable.[14]

On the other hand, like most single phased photocatalysts, Bi_xO_y suffers from poor charge separation which can hinder the photocatalytic efficiency.[11] To overcome this drawback, composite heterojunction materials based on Bi_xO_y have been developed, including Bi_2O_4–Bi_4O_7–BiO_{2-x}, Bi_2O_4/BiO_{2-x}, Bi_2O_4/$Bi_2O_2CO_3$, Bi_2O_3/Bi_2O_4, m-Bi_2O_4/Fe_2O_3,[11,22–25] and improved photocatalytic performance has been demonstrated. Loading transition metal nanoparticles onto semiconductor surface has been well known as an effective approach to improve the charge separation and quantum efficiency through IFCT and plasmon resonance mechanisms.[10,26] It is a relatively simple technique as compared to the preparation of heterojunction materials. One of the well-known method in producing metal nanoparticles is using the borohydride reduction method.[27] Since the reduction process can have a negative impact on the structure of the photocatalysts, chemically stable photocatalysts are more suitable for this technique. TiO_2 loaded with either Au or Ag have shown an enhancement in their photocatalytic properties mainly due to better charge separation and a slight red shift due to presence of metallic nanoparticles.[26] It is expected that Au/Ag transition metal loading *via* the borohydride reduction method would be suitable in improving the charge separation and sensitivity of Bi_2O_4 and enhance its efficiency in azo dye waste water treatment under visible light.

Therefore, in this paper, Au/Ag metal nanoparticle/cluster loading onto Bi_2O_4 was investigated. Our results showed significant improvement in the dye degradation properties *via* the degradation of a common azo dye, *i.e.*, methyl orange (MO). Both Au and Ag loaded Bi_2O_4 (Au–Bi_2O_4 and Ag–Bi_2O_4) exhibited enhanced photodegradation rate and increased quantum efficiency shown by their respective photocurrent and photodegradation measurements.

2. Experiment

2.1 Synthesis of modified Bi_2O_4

Dibismuth tetraoxide (Bi_2O_4) was synthesized using sodium bismuthate dihydrate ($NaBiO_3 \cdot 2H_2O$, 99.9%) of analytical grade. $NaBiO_3 \cdot 2H_2O$ (1.12 g) was dissolved in 60 mL of deionized water (DI) in a 100 mL beaker and stirred for 40 minutes followed by adding to a Teflon lined autoclave. The Teflon lined autoclave was maintained at 180 °C for 4 h. An orange precipitate was formed which clouded the liquid mixture with its fine particles. The autoclaved product was transferred into a beaker followed by a thorough flushing with deionized water to ensure the complete transfer of the prepared Bi_2O_4. Due to the dense nature of Bi_2O_4, water was easily decanted and the obtained product was rinsed with DI water twice and decanted again in a water bath. Finally, the sample was rinsed with ethanol and left to dry in a drying oven.

To synthesize the modified Bi_2O_4 (Ag/Au nanoparticle loaded) the borohydride reduction method was used. A fixed amount of pure Bi_2O_4 was continuously added while the borohydride reaction was in the process for synthesizing Ag or Au nanoparticles, so that the metal nanoparticles would be grafted as nanoclusters onto the surface of Bi_2O_4. The detailed synthesis has been carried out through the following process. First add 0.2 g of Bi_2O_4 into 60 mL deionized water in a 100 mL beaker along with continuous stirring for 30 minutes at 600 rpm. An aliquot of $AgNO_3$ or $HAuCl_4$ solution with specified molar concentration was added to get the target mass% ratio to each Ag–Bi_2O_4 and Au–Bi_2O_4 samples. The mixture was further stirred for 30 minutes, followed by the addition of $NaBH_4$ solution with the proper volume to precipitate the Ag or Au nanoparticles. Finally, the mixture was stirred for 2 hours to ensure that most of the $AgNO_3$ or $HAuCl_4$ reacted with $NaBH_4$. The mixture was left to decant so that the solid particles settle down, followed by washing with DI water and then with ethyl alcohol. The samples were transferred to a Petri dish, dried on a hotplate at 60 °C and then collected.

2.2 Characterization

The phase structure of the samples was characterized *via* X-ray diffraction by XRD apparatus (Rigaku MiniFlex 600 X-ray diffraction (XRD)) using a Cu K_α (0.15418 nm) radiation. Sample morphology was measured using a high-resolution transmission electron microscope (HRTEM, JEOL, JEM-3000F). Further characterization was performed by XPS using a mono-chromated Al K_α X-ray source ($h\nu = 14$ 86.6 eV) at 15 kV/150 W. The spot size used was 400 mm (Theta Probe AR-XPS System, Thermo Fisher Scientific, Waltham, MA, USA). In addition to characterization, XPS was also used to measure the valence spectra of both Ag and Au loaded Bi_2O_4.

2.3 Optical, photocatalytic and photochemical properties

Optical properties (optical band gap energy) of the samples were measured using UV-visible spectrophotometer (Jasco Inc. – UV/vis/NIR-spectrometer V-570). The absorption spectra were measured within the visible light spectrum (400–700 nm) for each sample. Optical band-gap energy was determined from the absorption spectra using the Tauc plot method.

To analyze the photocatalytic efficiency, methyl orange was chosen as the model pollutant. A stock solution of MO (20 ppm) was prepared, and 50 mL of this solution was transferred to a non-reflective transparent cylindrical reactor. Initially an

aliquot of 3.5 mL MO solution was extracted as the control sample and to the rest of the solution 50 mg of the sample photocatalyst was added. The cylinder was fully wrapped with aluminum foil and stirred for 30 minutes at 900 rpm to make sure the solution was in equilibrium before exposing to the visible light. The light source was provided by a 150 watt "warm" sodium vapor lamp. 3.5 mL samples were extracted from the photocatalyst–MO solution at 20 minute intervals for a duration of 120 minutes. Thus a total of 8 samples (including control sample) were extracted. This procedure was repeated for all Au/Ag–Bi_2O_4 loaded samples. To investigate reusability of the composite material three consecutive runs experiment was performed. For this purpose, an aliquot of MO stock solution was mixed with 45 mL DW containing the photocatalyst (1 g L^{-1}). The rest of the procedure was same as mentioned before, with exception that at each interval 1 mL of sample was collected. Furthermore at the end of each run a new sample from stock solution was added into the system with no further addition of the composite material. The relative concentration of MO of each photocatalyst–MO sample was measured using the UV-vis spectrophotometer (Agilent hp 8453 liquid spectrophotometer). The photodegradation curve for each sample was plotted in accordance with Beer–Lambert's law.

The production of the reactive oxygen species (ROS) involved in the photodegradation process were determined by introducing scavenger ions into the photocatalyst–MO solution. *p*-Benzoquinone, methanol, and EDTA-2Na were used to scavenge the ROS *i.e.* O_2^-, $^{\bullet}OH$ radical, and holes (h^+), respectively.[11] For this purpose, 3.5 mL scavenger solution (10 mmol of each benzoquinone, methanol, and EDTA-2Na) was added to the 50 mL sample solution after extracting the control sample. The rest of photocatalytic experiment was performed same as mentioned above. The effect of the scavenger ions was analyzed by measuring the changes in the MO concentration of sample solution.

Photochemical properties such as the photocurrent and the impedance were measured using an electrochemical workstation (Ivium Technologies Compactstat. Electrochemical Workstation) which is a three-electrode system potentiostat. A Pt plate and an Ag/AgCl electrode (in saturated KCl) were used as the counter and the reference electrode, respectively. The photocurrent *vs.* time curves were measured using 1.0 M Na_2SO_4 solution at room temperature and a 150 W LS150 light source from Abet Technologies.

3. Results and discussion

The XRD pattern of Bi_2O_4 loaded with either Ag or Au suggest that there is little to no change in the lattice structure of Bi_2O_4, since there is no obvious shift in the XRD peaks that belong to Bi_2O_4 (PDF, no. 50-0864) (Fig. 1). On the other hand, there were additional phases detected starting from both 5% Au–Bi_2O_4 and 5% Ag–Bi_2O_4 (labeled by * in Fig. 1). At higher concentrations (>5%) of prerequisites of Ag or Au, these peaks became more discernable, which suggest that they belong to the products of the borohydride reduction process as it is the only variable that was changed.

In Fig. 1a, these peaks were identified to be metallic Ag (PDF, no. 04-0783) which indicates the formation of pure silver. Judging from the peaks shape, it indicates low crystallinity due to the relatively low intensity and broad Ag peak. The structure of the pure Ag indicated by its PDF card is a cubic $Fm\bar{3}m$ face-centered structure, since it is an indexable peak. Similarly, in Fig. 1b, the peaks were identified to be metallic Au (PDF, no. 04-0784). It also shows low crystallinity judging from its intensity and peak shape. Its structure is cubic $Fm\bar{3}m$ face centered lattice structure according to its PDF card.

From the XRD analysis it can be concluded that during the borohydride reduction, Ag or Au metallic nanoparticles were produced. More accurate chemical analysis of the nanoparticles was investigated through the XPS measurement (see later discussion). Also, it can be inferred that during the reduction process it did not change the lattice structure of the Bi_2O_4 material. Instead, the reduced metallic atoms were loaded onto the surface of Bi_2O_4 as nanoclusters. This explains the negligible change in the lattice structure of Bi_2O_4, because changes to the lattice should be seen as discernable changes on its lattice parameters and thus the position of the XRD peaks.

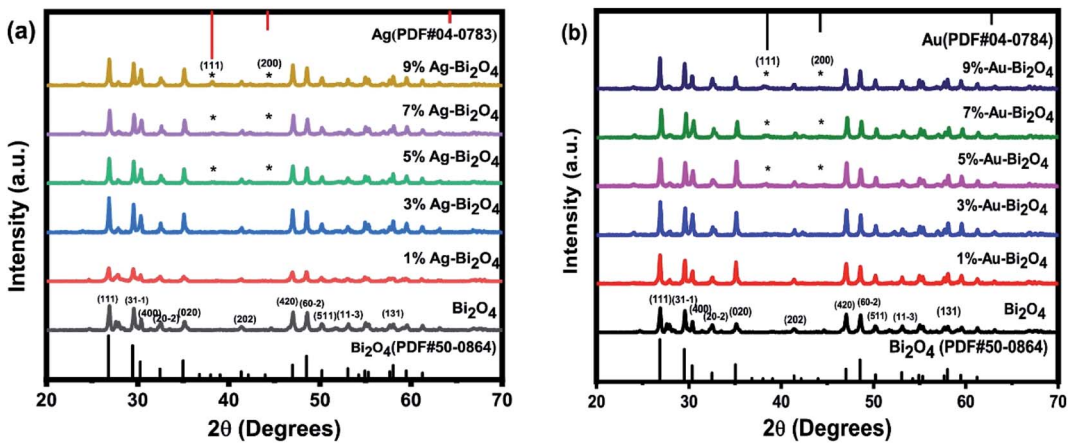

Fig. 1 XRD pattern of the prepared samples (a) Ag–Bi_2O_4, (b) Au–Bi_2O_4.

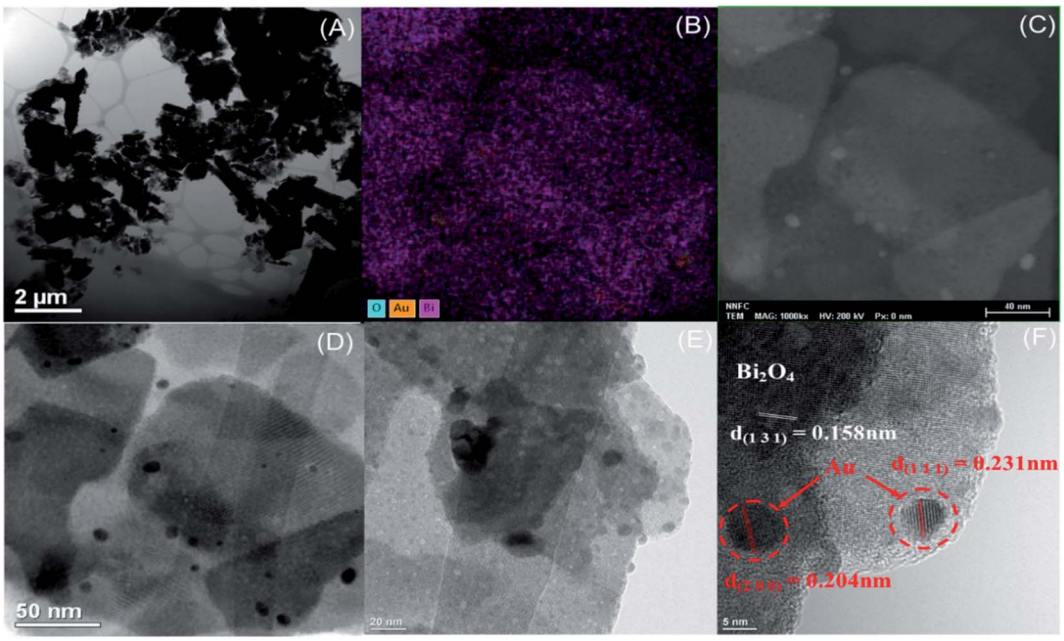

Fig. 2 TEM/HRTEM (A and C–F) and (B) element mapping of (7% Au–Bi_2O_4).

Furthermore, an addition of a new phase was observed which could be attributed to the possibility of metallic Ag/Au nanoclusters settled on the surface of Bi_2O_4.

To confirm that the metallic Au/Ag nanoclusters were loaded onto Bi_2O_4, elemental mapping and TEM/HRTEM measurements were employed on the samples with higher photocatalytic efficiency. The TEM results of 7% Au–Bi_2O_4 sample (Fig. 2A) showed that the structure retains Bi_2O_4 with the nanorod morphology. The presence of Au on the surface of Bi_2O_4 was confirmed from the elemental mapping in Fig. 2B. The Au nanoparticles on the surface of Bi_2O_4 were distinguished to be the black blotches in the HRTEM images (Fig. 2C–E). In the higher magnification image (Fig. 2F) the black blotches were confirmed to be metallic Au nanoclusters evidenced by its lattice fringe of 0.204 nm and 0.231 nm, which correspond to the lattice planes of metallic Au (200) and Au (111). This confirms the assumptions gathered from the XRD data as these planes belong to the indexed metallic Au PDF card.

For the Ag–Bi_2O_4 composites, the samples with Ag (1%) was found to have significantly enhanced photocatalytic efficiency. In Fig. 3, from the lower magnification (Fig. 3A and B) it is evident that the morphology of Bi_2O_4 remained unchanged as nanorod, similar to the results seen from the TEM images of the Au–Bi_2O_4 (Fig. 2). The nanorod size in this particular result was 700 nm. In Fig. 3C, metallic Ag nanoparticles can be clearly seen. The lattice fringe of the nanoparticle cluster is 0.242 nm as shown in Fig. 3D, which corresponds to the lattice plane of (111) metallic Ag as indexed from the XRD data shown earlier (Fig. 1a). Therefore, similar to Au–Bi_2O_4, it was observed that metallic Ag nanoclusters were formed on the surface of the Bi_2O_4 nanorods.

To analyze the effects of the changes in the morphology, structure, and composition to the overall efficiency of the modified materials, the photodegradation efficiency of each sample was evaluated. The photodegradation rate curves were determined by photodegrading 20 ppm of methyl orange (Fig. 4). The photodegradation rate was determined using the first order quasi reaction equation.

Fig. 4a shows that Ag–Bi_2O_4 had enhanced degradation efficiency for 20 ppm MO under visible light irradiation for

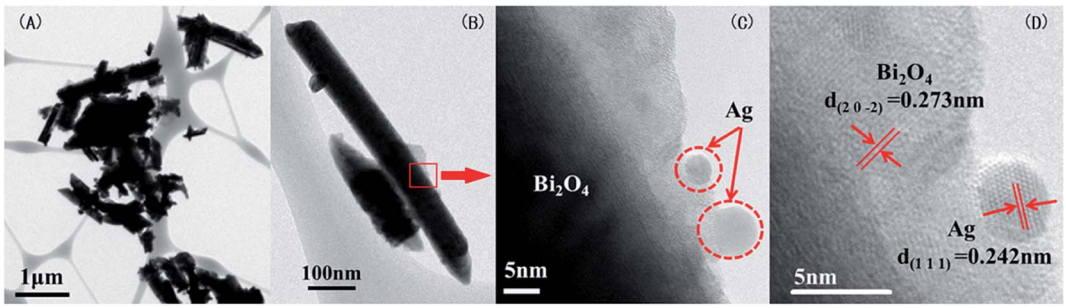

Fig. 3 TEM and HRTEM snapshots (A–D) of (1% Ag–Bi_2O_4).

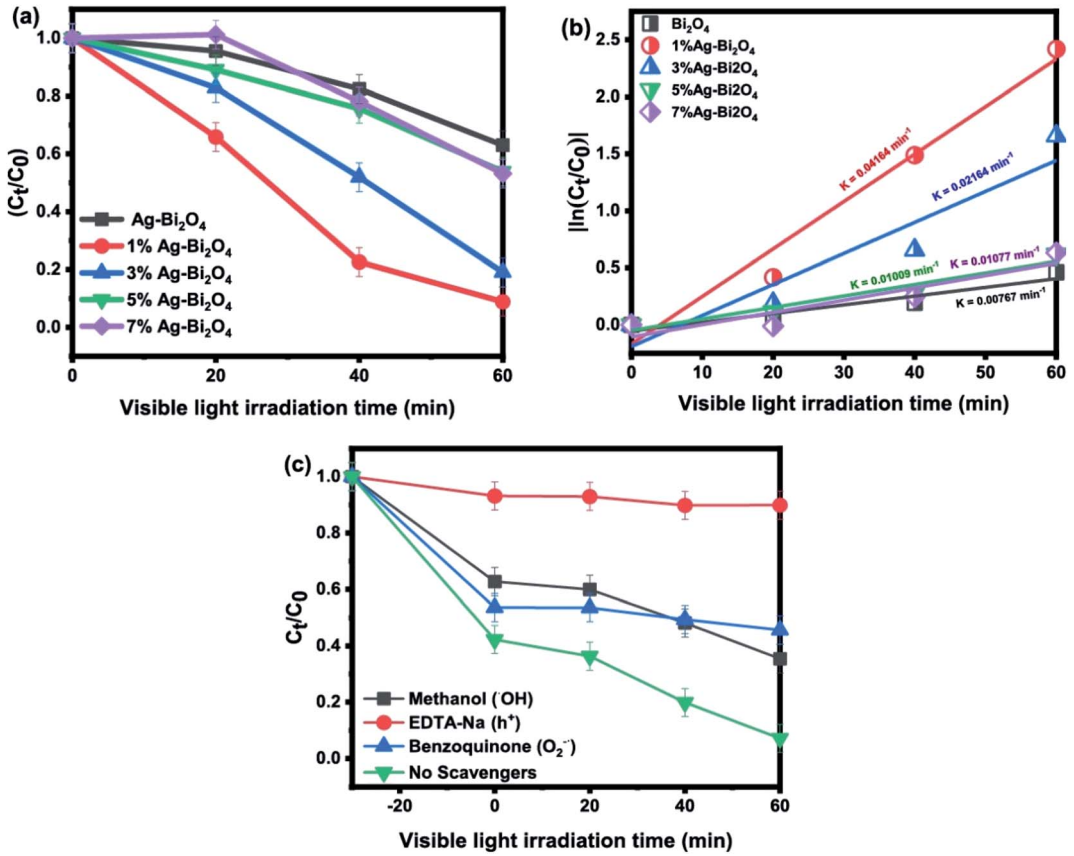

Fig. 4 (a) Photodegradation curve of MO by Ag–Bi_2O_4, (b) quasi first order reaction rates, (c) scavenger ion experiments.

60 min as compared to the pristine Bi_2O_4. Particularly, 1% Ag–Bi_2O_4 exhibited the highest photodegradation rate than Bi_2O_4 loaded with 3, 5, and 7% wt-Ag. In Fig. 4b, by determining the reaction rate of each sample it was found that the 1% wt Ag–Bi_2O_4 had the highest photodegradation rate (0.04164 min^{-1}), which is about 5.4 times faster than that of the pristine Bi_2O_4 (0.00767 min^{-1}). The scavenger study (Fig. 4c) shows that EDTA-Na completely inhibited the photodegradation process by impeding the formation of holes (h^+), indicating that hole (h^+) was the major contributor in photodegradation process. Similarly, the effect of benzoquinone implied that $O_2^{\cdot}$ also plays a major role. However, the scavenging pattern of methanol shows that though initially it hold the reaction from taking place it could not control the reaction for longer due to overwhelming role of holes (h^+) and $O_2^{\cdot}$ (Fig. 4c).

Fig. 5 displays the photodegradation of methyl orange by Au–Bi_2O_4. Obviously, 7% Au–Bi_2O_4 exhibited the efficient photodegradation activity (Fig. 5a) with the highest degradation rate (0.05904 min^{-1}) (Fig. 5b). This value is 7.69 times faster than that of unmodified Bi_2O_4 and has degraded 63% more MO than pristine Bi_2O_4 in 60 min. Although there was difference in the degradation rate of the Au–Bi_2O_4 composites loaded with different Au loading (Fig. 5b), yet the total removal of MO was found to be similar *i.e.* more than 10% increased degradation than pristine sample. In Fig. 5c, the scavengers' effect showed that the major degrading reactive specie was holes (h^+). The effect of benzoquinone showed that $O_2^{-\cdot}$ radicals also play a key role in photodegradation of MO by Au–Bi_2O_4 (Scheme 1), whereas the ˙OH seemed having not much effect on the degradation process.

A major consideration for a photocatalyst is its stability and reusability for photodegradation of pollutants. Therefore, to show the stability of the as prepared material, photodegradation of MO under visible light irradiation was performed for three consecutive runs (Fig. 6). Results show that the photocatalytic efficiency remained almost stable for the first two runs but decreased in the third run down to about 85% for both composites (Fig. 6a and c). This decrease could be due to the catalyst inactivation by surface adsorption of small molecular entities during photodegradation. Furthermore, a little decline in the degradation ratio of MO can also be attributed to the loss of the catalyst during the recovery process. It is known that under the light illumination the high-valence bismuth in Bi_2O_4 tends to change into Bi^{3+}, that's why Bi_2O_4 generally has week photostability after the recycling experiment. Therefore, to investigate the structure stability of Bi_2O_4 in the samples, the composites were analyzed by XRD before and after the consecutive runs of MO photodegradation. Fig. 6b and d show the XRD data of 1% Ag–Bi_2O_4 and 7% Au–Bi_2O_4 respectively. The XRD pattern of 1% Ag–Bi_2O_4 and 7% Au–Bi_2O_4 before and after performing the photodegradation of MO shows no major differences which further assures the structural stability of the

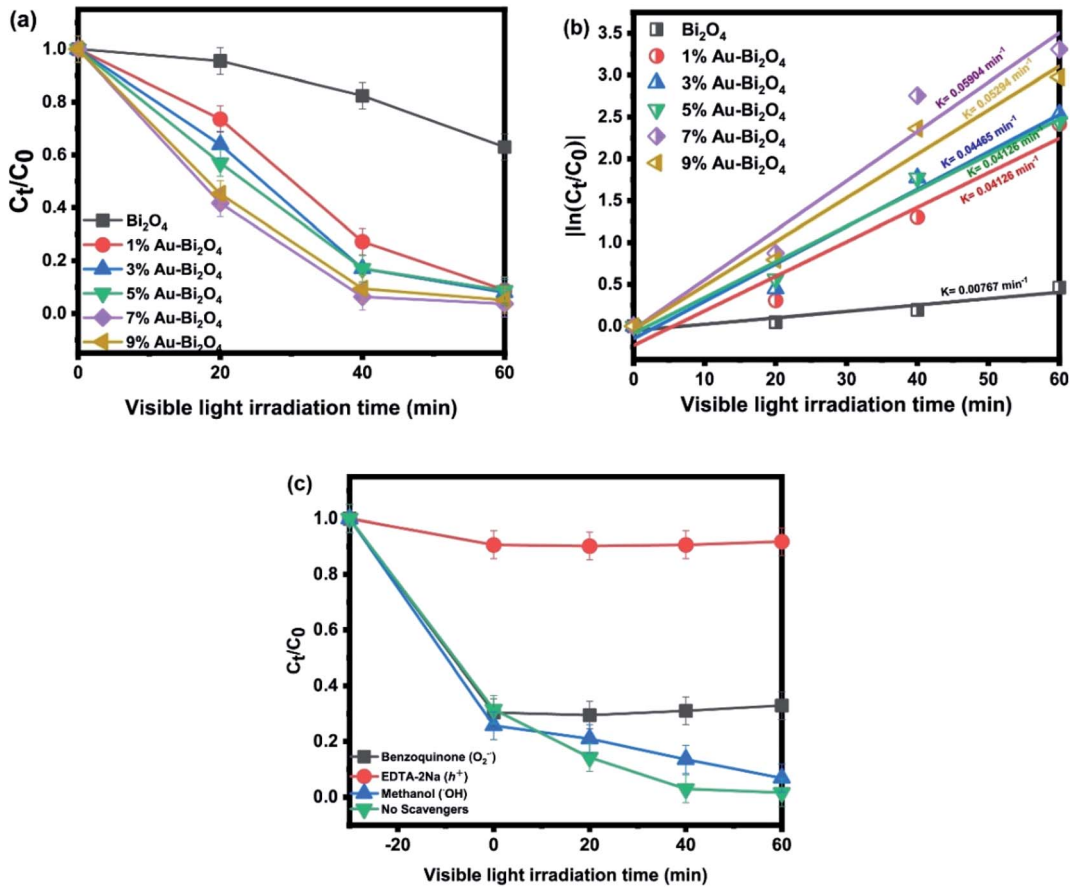

Fig. 5 (a) Photodegradation curve of MO by Au–Bi_2O_4, (b) quasi first order reaction rates, (c) scavenger ion experiments.

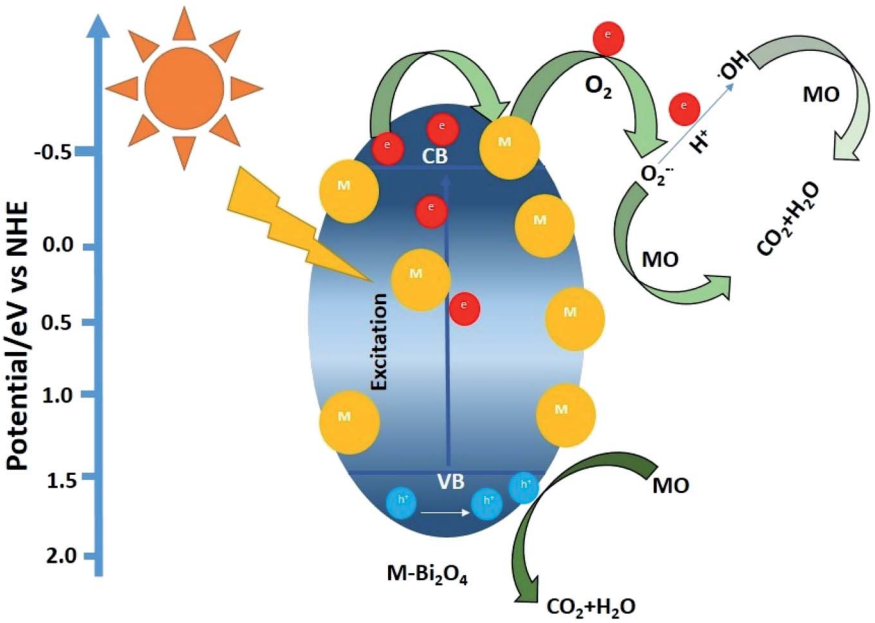

Scheme 1 Illustration of charge transfer between Bi_2O_4 and nanoclusters, and photocatalytic MO degradation by M/Bi_2O_4 under visible light irradiation (M = Ag or Au).

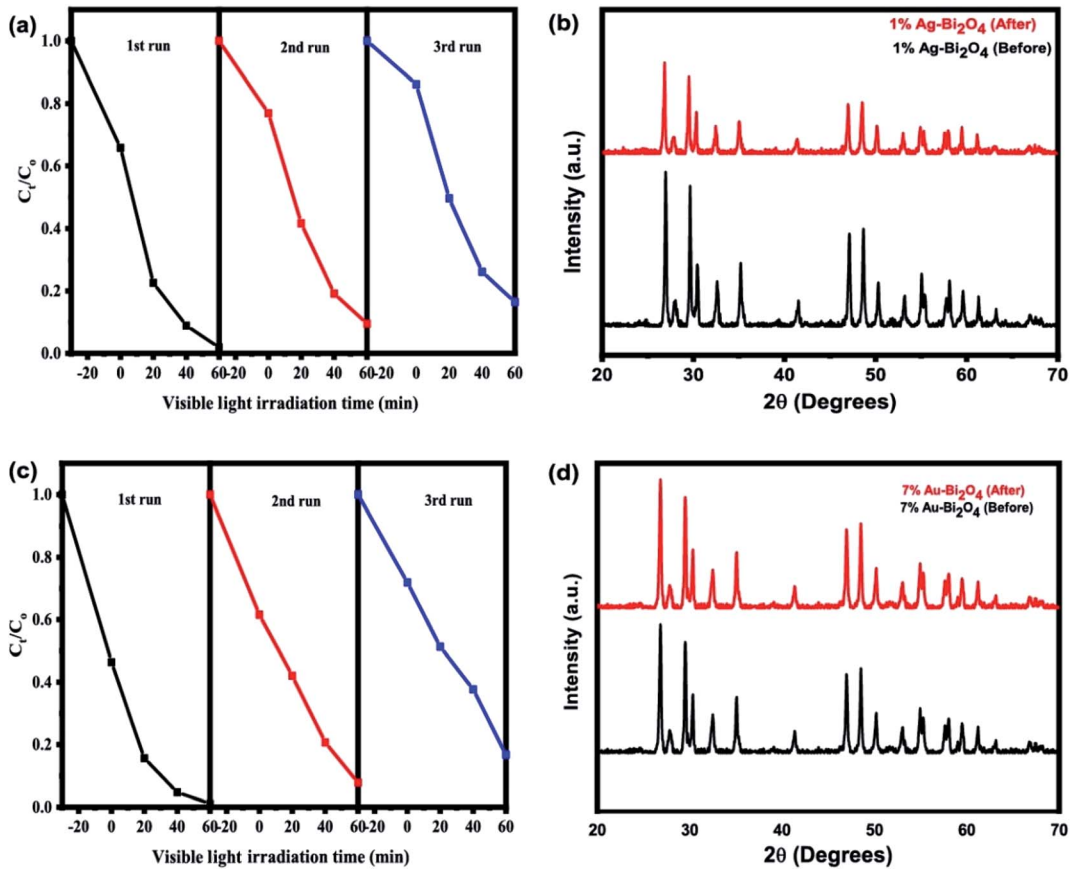

Fig. 6 Consecutive runs of (a) Ag–Bi_2O_4 and (c) Au–Bi_2O_4 for reusability, and XRD results before and after photocatalysis of (b) Ag–Bi_2O_4 and (d) Au–Bi_2O_4.

as prepared photocatalysts. The photo-stability and robustness of the composites could be ascribed to the enhanced separation and transfer of photo-induced charges which will be elaborated in the coming sections describing optical and photoelectric properties.

Since the chemical states of an element can provide insights to the photocatalytic property, the XPS measurement was employed to analyze the modified Bi_2O_4 composites (7% Au–Bi_2O_4). The XPS survey spectrum in Fig. 7a confirmed the presence of bismuth, oxygen, and gold species. From the high resolution XPS (Fig. 7b) the Bi 4f/7 spectra can be deconvoluted as 4 peaks that belong to the oxidation states Bi(III) and Bi(V) at 158.47 eV and 158.83 eV, respectively. In addition, due to spin orbit splitting, the Bi(III) and Bi(V) oxidation states occur at 163.64 eV and 164.24 eV as well. The deconvolution of the Au 4f/7 spectrum showed two peaks at 83.7 eV and 87.4 eV as shown in Fig. 7c. The peak at 87.4 eV is the spin orbit splitting peak of Au 4f/7.[28] Thus the XPS spectrum further confirmed the existence of metallic Au in the Au–Bi_2O_4 composite, which is consistent with the XRD results.

As for the oxygen O1s spectra (Fig. 7d) the peak at 529.5 eV normally accounts for the lattice oxygen in the form of an anion O_2^-.[29] As it is well documented for TiO_2, it is usually strong for metal oxides especially for transition metal oxides. The peak at 530.7 eV is attributed to dissociative O^- ions or oxygen vacancies.[30] This result means that there could be more defects on the surface of the material caused by the vacancy of the oxygen from the lattice. This change leads to an increased photocatalytic efficiency. The implications of the increase of oxygen vacancies in photocatalysis is beneficial as the correlation of oxygen vacancies to the efficiency of photocatalysts has been well documented. The increase in oxygen vacancy promotes better charge separation as the vacancies cause defect levels slightly lower than the band positions that in turn improves charge separation because the photoinduced hole and electron pair move to these vacancies before rejoining together.[11]

The survey graph for the XPS results for the 1% Ag–Bi_2O_4 (Fig. 8a) shows the presence of elemental Bi, O and Ag species with accurate percent composition of the material, concurrently. The Ag was shown to be 0.11% which is lesser than the amount of Ag material projected to achieve. It can be seen in Fig. 8b that the Bi $4f_{7/2}$ peak in the Bi_2O_4 can be fitted well to two peaks which is centered at the binding energies 163.53 and 163.91 eV. Like the 7% Au–Bi_2O_4 composite, the peaks situated at these binding energy positions can be attributed to Bi(III) and Bi(V) species, respectively. These peaks also correspond well to the Bi spin–orbit peaks of Bi_2O_4. However, slight difference was found when comparing the bi-modal peaks of Bi between Ag–Bi_2O_4 and Au–Bi_2O_4 samples, that is, the peak at 158.63 eV

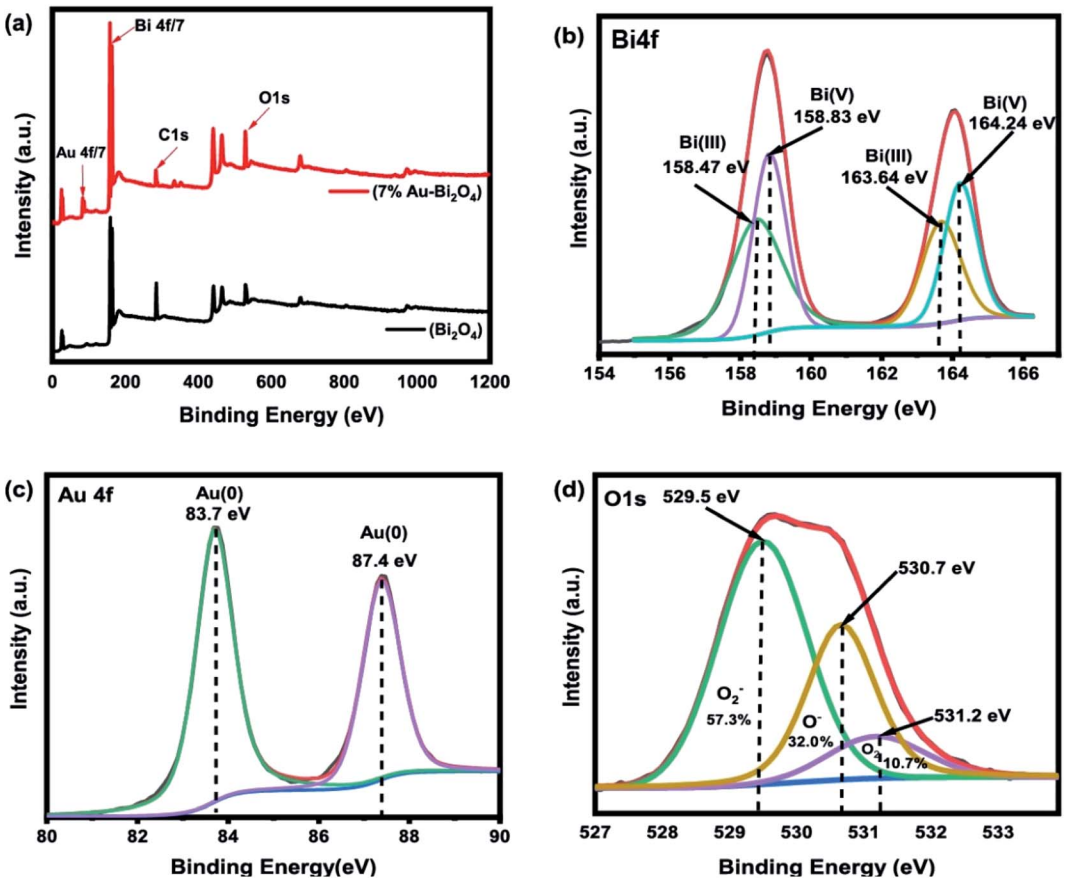

Fig. 7 XPS results of 7% Au–Bi_2O_4, (a) XPS survey, (b) Au4f spectra, (c) Bi4f spectra, (d) O1s spectra.

intensity is slightly lower but it is compensated for the increase in the area under the peak such the Bi^{3+} and Bi^{5+} maintaining approximately 1 : 1 ratio in their quantity in the Ag–Bi_2O_4 material which is expected, as there was no change in the chemical bonding of Bi_2O_4.

As for the silver Ag3d XPS spectra (Fig. 8c) it has been found that two peaks, which were fitted well, were situated at 367.44 eV and 373.35 eV that are in proper accordance with metallic Ag. The spin orbit splitting explains the 2 peaks of $Ag3d_{3/2}$ and $Ag3d_{1/2}$ which are also in proper accordance with a spin orbit energy difference of 6.0 eV.[28] The O1s spectra (Fig. 8d) shows 3 peaks as described earlier. The peaks shown in this figure are in good accordance with the O1s spectra of typical metal oxides. Like the O1s spectra of Au–Bi_2O_4, the Ag sample has chemi-absorbed oxygen present and also a lower quantity of O_2 defects and higher quantity of lattice O_2 according to the area under the deconvoluted peaks. Regardless, of these results from its O1s spectra, it can still be concluded that Ag nanocluster grafted Bi_2O_4 (Ag–Bi_2O_4) was properly synthesized, the only difference is that there are more O_2 vacancies present in the 7% Au–Bi_2O_4 composite.

The diffuse reflectance UV-visible spectra (UV-VIS DRS) were used to determine the bandgap values for each sample and its photosensitivity. From the UV-VIS DRS measurement the absorption edge of the pristine Bi_2O_4 was found to be 550 nm which is within the visible range and is confirmed by its ability to photodegrade MO (Fig. 4a and 5a). The addition of Au nanoclusters on to Bi_2O_4 improved its visible light absorption *via* red shift from 550 to 595 nm (Fig. 9a). Consequently, the Tauc plot (Fig. 9b) shows that the addition of Au nanoclusters decreased the band gap energy from 2.26 eV of the pristine Bi_2O_4 to 2.09 eV of the modified sample (Au–Bi_2O_4).

The increased sensitivity of the photocatalyst could be attributed to the increase of the oxygen vacancies. An increase of oxygen vacancy has been reported to induce a red shift in ZnO after annealing.[31] The oxygen vacancy adds defect levels that act as donor states under the conduction band thus narrowing the band gap energy. Hence it could be assumed that the same phenomena are happening with 7% Au–Bi_2O_4 because of the significant increase in oxygen vacancies.

Fig. 9c shows the absorption edges for 1% Ag–Bi_2O_4 sample along with the unmodified Bi_2O_4. It is evident that the higher absorption occurs around 500 nm and the overall shape of the absorption edges are the same. This could be attributed to the fact that there is no internal change in the Bi_2O_4 lattice as indicated by the XRD measurements, the TEM and HRTEM micrographs. However, a subtle change in the "tail" of the absorbance spectra can be observed, which is a common feature of surface modified photocatalyst.

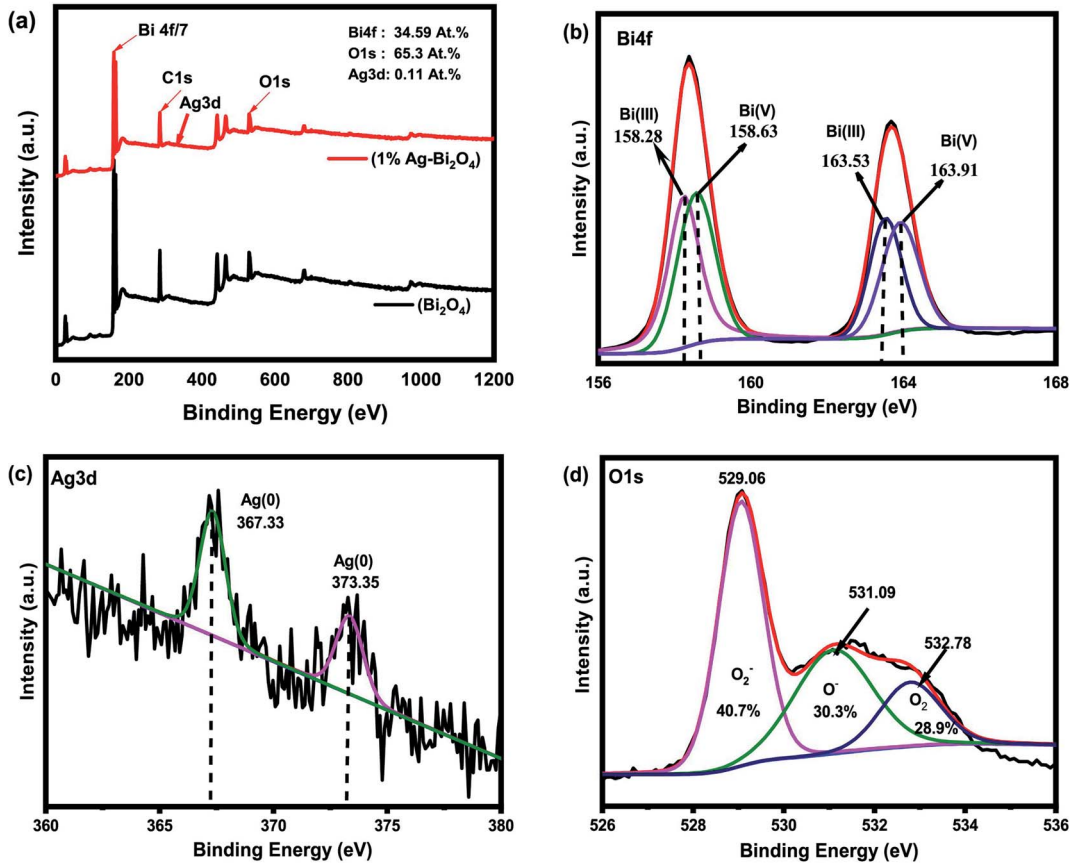

Fig. 8 XPS results of 1% Ag–Bi_2O_4, (a) XPS survey, (b) Bi4f spectra, (c) Ag3d spectra, (d) O1s spectra.

Consequently, the change in the absorption edge corresponds to a subtle change in the band gap energy of the modified Ag–Bi_2O_4 sample. Therefore, the band-gap energy was measured to be 1.9693 eV for the 1% Ag–Bi_2O_4 composite and 2.0346 eV for the pristine Bi_2O_4. The addition of Ag nanoclusters on the surface of Bi_2O_4 slightly decreased its band gap, which is also evident in the slight change of color of the Bi_2O_4. The results obtained could be useful in the formulation of the proposed band structure and ultimately the proposed photodegradation mechanism.

To gather insight for the increased efficiency of the samples, the photocurrent and EIS spectra were measured (Fig. 10). As for Ag–Bi_2O_4 samples it seems to be in accordance with what was observed in the photodegradation curve (Fig. 4a). The 1% Ag–Bi_2O_4 has both the most efficient degradation curve and fastest rate as well the most photocurrent output between all the Ag–Bi_2O_4 composite (Fig. 10b). The 1% Ag–Bi_2O_4 possess the output of around 3.3 nA which is 6.6 times higher than the unmodified Bi_2O_4. This is also in line with the charge transfer mechanisms in which it improves charge separation and conductivity, and consequently improves the production of charged species. However, no direct relation can be seen in the increase of Ag nanoclusters to its photocurrent output. But the decrease in the photocurrent output may explain the inefficiency of the higher Ag concentration.

Fig. 10c shows that 3% Au–Bi_2O_4 composite has the lowest impedance compared to all the samples including Ag–Bi_2O_4 and unmodified Bi_2O_4. In Fig. 10d it follows that it has the highest photocurrent of around 1.1 nA, suggesting that it would produce more reactive oxygen species. However, it is contrary to the behavior shown in the photodegradation experiment (Fig. 5a and b) which shows that 7% wt Au–Bi_2O_4 was the most efficient photocatalyst. The photocurrent explains the increased photodegradation rate from the pristine samples up to the 3% Au–Bi_2O_4 sample. However, the degradation rate increases continuously as the Au concentration is increased above 3%, which is contrary to the change in the photocurrent results. These contradictory results are explained below.

An explanation of the recession of the photocurrent values after reaching a certain concentration of Au (3%) could be due to the size of the Au nanoclusters. It has been reported that when Au nanocluster reach a size of >5 nm the photocurrent density starts regressing due to the decrease in surface area of Au nanoparticles that photocatalyst needs to expose to the electrolytic solution.[9] At the same time the amount of surface in which radiation can reach to the material is being blocked by the "big" Au nanoclusters. This phenomenon can also be used to explain the Ag samples photocurrent regression. Furthermore, a certain ratio between $HAuCl_4$: $NaBH_4$ should be maintained to synthesize 5 nm gold nanoparticles which is the appropriate size to not to block the irradiation or inhibit the

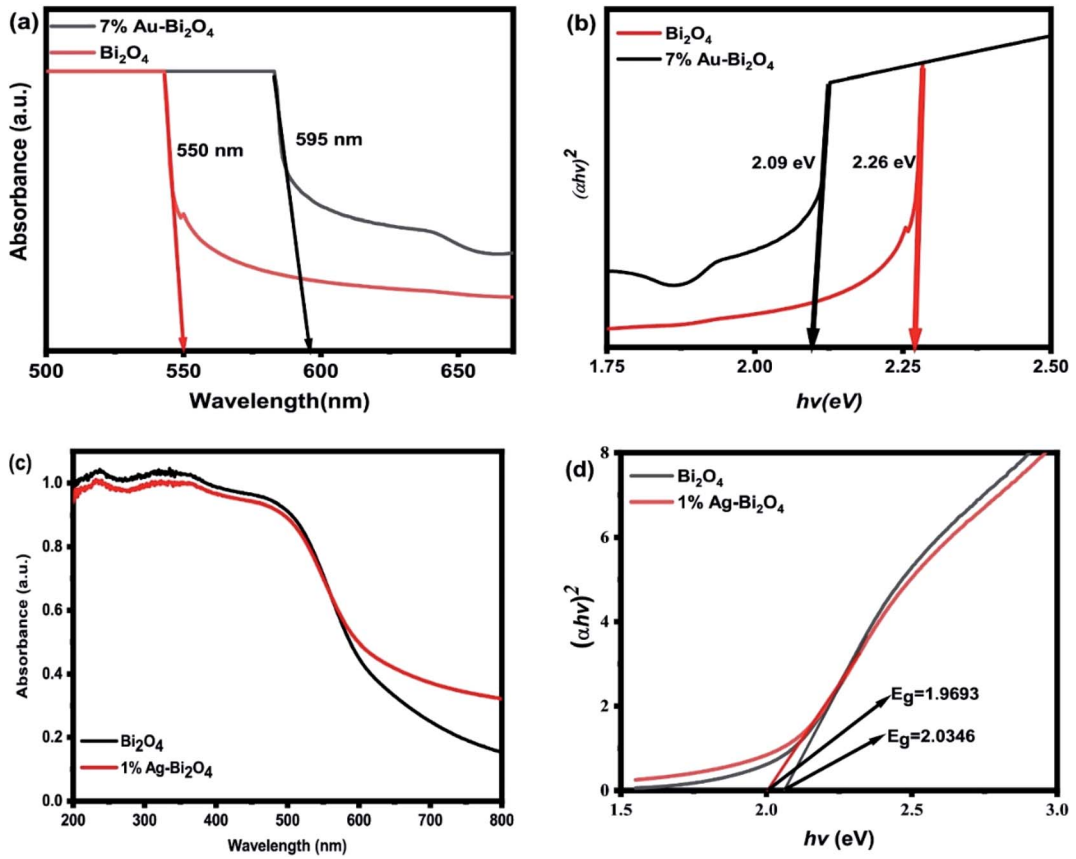

Fig. 9 UV-VIS DRS of (a) 7% Au–Bi_2O_4, (c) 1% Ag–Bi_2O_4 and Tauc plots of (b) 7% Au–Bi_2O_4 and (d) 1% Ag–Bi_2O_4.

induction of transients (current).[32] Accordingly,[9] it has been shown that with a solution with a ratio of 10 equiv. per atom. Au will be in a colloidal form of suspended 3 nm gold nanoparticles.[9] If there is an excess of $NaBH_4$ the solution is more likely to precipitate "big" clusters of Au or Ag which will be detrimental to the photocurrent capability of the material.

However, this does not explain the better photodegradation ability of higher Au concentrations (>3%). Still, it can be assumed that the increased O_2 vacancies is the reason why at higher Au concentrations the material remains efficient and further improves its efficiency. Observations when comparing Ag to Au samples support this, as the XPS measurement shows higher O_2 vacancies since it is the only chemical difference seen between the Au/Ag samples besides the obvious different surface loaded atoms. Also in the UV-VIS DRS measurement a more noticeable redshift was seen which is similar to the previous literature.[31] The dominant effect of the higher O_2 vacancies on the photocatalytic efficiency can be understand as that, the sample has enough O_2 vacancies to offset the recessed photocurrent. Thus, these oxygen vacancies can become active sites where the photoinduced species are likely to react to the absorbed degradant due to higher-than-normal defect levels.[11]

To give an accurate depiction on how the Au/Ag grafted Bi_2O_4 perform their photodegradation processes, the band positions are to be determined at first. To accurately hypothesize their band positions, measuring the valence edge from the valence spectra of each material in the XPS process, their optical band-gap (determined earlier) and the material's work function are needed. In conjunction to these parameters a series of equations were used to determine the valence band and conduction band of each material.

The valence spectra of each material are shown in Fig. 11. To determine the valence edge, a region of the spectra near 0 eV is of interest where the "edge" of the valence spectra could be seen. If a line is drawn overlapping the edge such that it intersects the ($y = 0$) X-axis (binding energy), the value that it intersects is the valence edge of the material.

The valence edge of 7% Au–Bi_2O_4 material is 1.17 eV while 1% Ag–Bi_2O_4 material is 0.97 eV. The work function of unmodified Bi_2O_4 used was 5.22 eV,[11] while the band gap energy as determined earlier are 2.03 eV and 2.09 eV for 1% Ag–Bi_2O_4 and 7% Au–Bi_2O_4 respectively. The conduction band and valence band were calculated using the following equations:[33,34]

$$-E(\text{avs})_{\text{v}} = \phi_{\text{work function}} + \chi_{\text{valence band}} \quad (1)$$

$$E(\text{avs})_{\text{c}} = E(\text{avs})_{\text{v}} + E_{\text{g}}\ (\text{band gap}) \quad (2)$$

$$E(\text{NHE}) = -E(\text{avs})_{\text{c or b}} + (-4.5\ \text{eV}) \quad (3)$$

For 7% Au–Bi_2O_4 the calculated band structure was determined to be +1.89 eV and −0.2 V(NHE) for the valence band and conduction band respectively. And for the 1% Ag–Bi_2O_4 sample

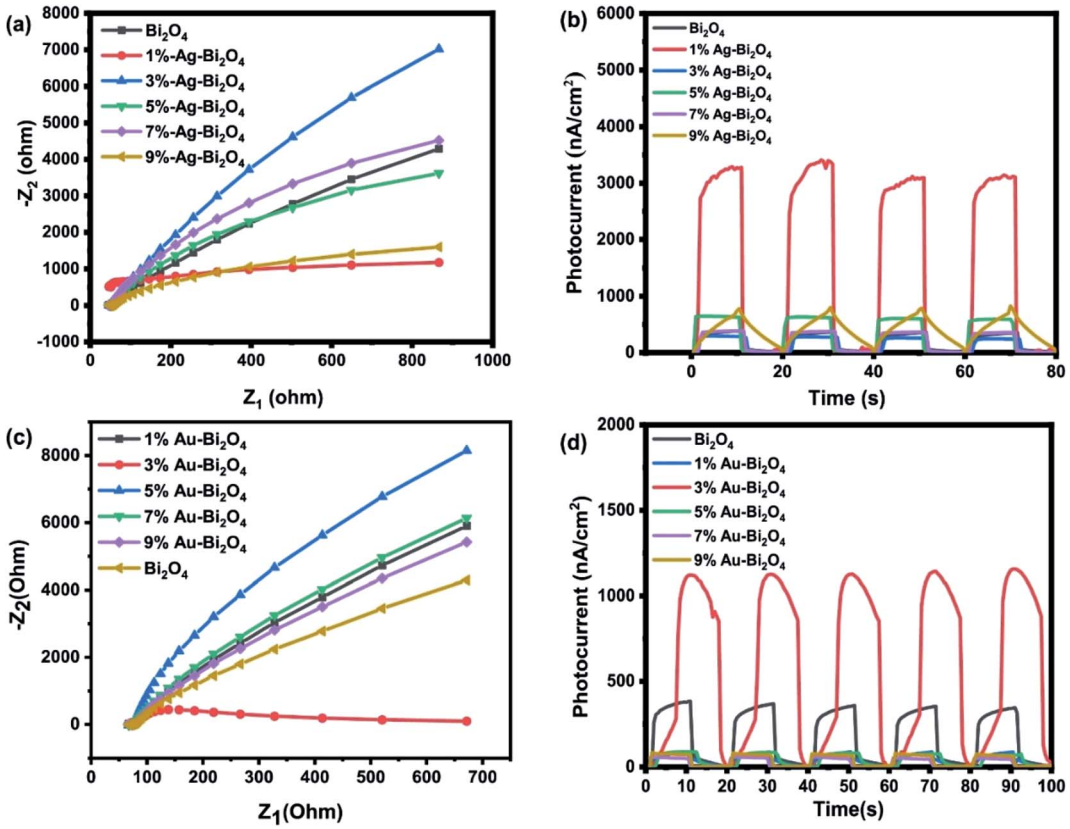

Fig. 10 EIS spectra of (a) Ag–Bi_2O_4 and (c) Au–Bi_2O_4, photocurrent graph of (b) Ag–Bi_2O_4 and (d) Au–Bi_2O_4.

its valence band and conduction were calculated to be +1.69 V (NHE) and −0.34 V (NHE) respectively.

Having determined the band positions of the samples developing mechanism was the next step to understand the processes involved in the photodegradation of the methyl orange or azo dyes in general. From the scavengers' analyses, it has been concluded that the major reacting specie involved in the photodegradation process is the hole (h^+). In addition, superoxide species and hydroxyl species were also detected, but they were not the major oxidizing species.

Therefore, as the mechanism was hypothesized it was considered whether the calculated band positions could generate the reactive species first.[11] At band position less than −0.33 eV *vs.* NHE, which is reduction potential of O_2^-, the photocatalyst can generate superoxide species O_2^- which can photodegrade methyl orange as well.[11] Thus, the calculated conduction band for the Ag supported the involvement of superoxide O_2^- species, as detected in the scavenger experiments. Similarly, the oxidation potential is not positive enough to generate hydroxyl species (OH^-) directly.[11] Therefore, the

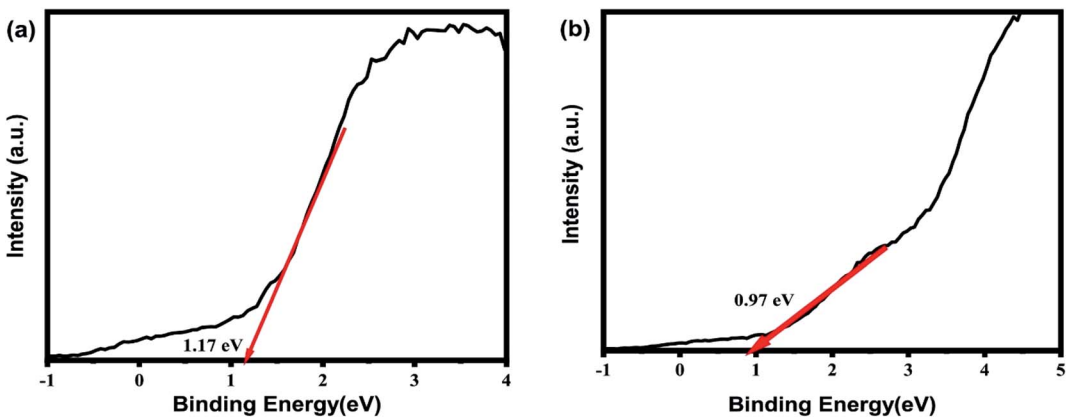

Fig. 11 Valence spectra of (a) 7% Au–Bi_2O_4, (b) 1% Ag–Bi_2O_4.

valence band of 1% Ag–Bi_2O_4 and the 7% Au–Bi_2O_4 samples were not able to generate hydroxyl species (OH^-) in high quantities which is evident from the scavenger experiments of the two samples.

Taking all the aforementioned characteristics into consideration, the mechanism could be hypothesized as:

Initiation of photocatalytic reaction:

$$Bi_2O_4 + h\nu \rightarrow e^- + h^+ \text{ (hole)}$$

On the valence band, direct oxidation by positive hole.

$$\text{Dye} + h^+ \rightarrow \text{dye}_{ox} \text{ (oxidized)}$$

Conduction band electron trapped by oxygen

$$O_2 + e^- \rightarrow O_2^-$$

Subsequent production of hydroxyl species due to the occurrence of superoxide.

$$^{\cdot}O_2^- + H^+ \rightarrow {}^{\cdot}HO_2$$

$$^{\cdot}HO_2 + e^- \rightarrow HO_2^-$$

$$HO_2^- + H^+ \rightarrow H_2O_2$$

$$H_2O_2 + e^- \rightarrow {}^{\cdot}OH + OH^-$$

Thus, when the photocatalyst was irradiated, the photogenerated electrons and holes were produced. Due to their respective band positions, both were able to degrade the target material *via* direct oxidation using the photogenerated holes. Secondly the scavenger experiments confirmed that superoxide ions were produced in both samples. However, it is to be noted that since 7% Au–Bi_2O_4 has a calculated conduction band of −0.2 V *vs.* NHE, it cannot possibly produce superoxide ion. This discrepancy can be understand considering the existence of the O vacancies and the Au nanoclusters. It is well known that the addition of Au can change the surface work function and at the same time oxygen vacancies create defect levels that could alter the final band positions.[10,11,31] Therefore, the actual conduction band of 7% Au–Bi_2O_4 could be more negative than −0.33 V *vs.* NHE so that superoxide ions were produced. At the third part of the mechanism proposal, in both samples, the production of hydroxyl species can be explained by the presence of the superoxide ion as it can go two pathways, either directly degrading the dye, or reacting with protons in the solution and produces hydroxyl species that ultimately degrades the dye.

4. Conclusion

The addition of metallic Au/Ag nanoparticles/clusters on the surface of Bi_2O_4 enhanced its photocatalytic efficiency. On average, more than 10% increase in the total removal of MO and more than 6 times increase in the rate of degradation was observed in the modified photocatalysts. Two types of effects can be implicated from the experimental results. First, the crafting of Au or Ag nanoparticles can be effective in the separation of photogenerated charges and improve the photodegradation efficiency. Second, the oxygen vacancies can be created during the metal deposition process, which also plays an important role in determining the photocatalytic performance. Our results showed that more oxygen defects exist in 7% Au–Bi_2O_4, which may explain the obvious enhanced visible light absorption and MO degradation rate as compared with 1% Ag–Bi_2O_4. Recycling tests showed only slight decrease in the degradation efficiency with 3 repeated uses and no change in XRD spectra, indicating that the Au and Ag nanoparticle/Bi_2O_4 composite can be used as a stable visible light photocatalyst for azo dyes degradation.

Conflicts of interest

The authors have no conflict of interest to declare.

Acknowledgements

This research was supported by the Basic Science Research Program (2019R1A2C1086881) and the Nano-Material Technology Development Program (2009-0082580) through the National Research Foundation of Korea funded by the Ministry of Science, ICT and Future Planning.

References

1 A. Baban, A. Yediler, D. Lienert, N. Kemerdere and A. Kettrup, *Dyes Pigm.*, 2003, **58**, 93–98.
2 M. Sudha, A. Saranya, G. Selvakumar and N. Sivakumar, *Int. J. Curr. Microbiol. Appl. Sci.*, 2014, **3**, 670–690.
3 S. Hildenbrand, F. Schmahl, R. Wodarz, R. Kimmel and P. Dartsch, *Int. Arch. Occup. Environ. Health*, 1999, **72**, M052–M056.
4 R. O. A. de Lima, A. P. Bazo, D. M. F. Salvadori, C. M. Rech, D. de Palma Oliveira and G. de Aragão Umbuzeiro, *Mutat. Res., Genet. Toxicol. Environ. Mutagen.*, 2007, **626**, 53–60.
5 N. M. Julkapli, S. Bagheri and S. B. Abd Hamid, *Sci. World J.*, 2014, 692307.
6 P. A. Pekakis, N. P. Xekoukoulotakis and D. Mantzavinos, *Water Res.*, 2006, **40**, 1276–1286.
7 Y.-J. Xu, Y. Zhuang and X. Fu, *J. Phys. Chem. C*, 2010, **114**, 2669–2676.
8 Y. Zhang, J. Wan and Y. Ke, *J. Hazard. Mater.*, 2010, **177**, 750–754.
9 W. J. Chen, Y. H. Lu, W. Dong, Z. Chen and M. R. Shen, *Mater. Res. Bull.*, 2014, **50**, 31–35.
10 S. G. Kumar and L. G. Devi, *J. Phys. Chem. A*, 2011, **115**, 13211–13241.
11 Y. F. Jia, S. P. Li, H. Ma, J. Z. Gao, G. Q. Zhu, F. C. Zhang, J. Y. Park, S. Cha, J. S. Bae and C. Liu, *J. Hazard. Mater.*, 2020, **382**, 121121.

12 B. Frit and J. Mercurio, *J. Alloys Compd.*, 1992, **188**, 27–35.
13 R. A. He, S. W. Cao, P. Zhou and J. G. Yu, *Chin. J. Catal.*, 2014, **35**, 989–1007.
14 W. Wang, X. Chen, G. Liu, Z. Shen, D. Xia, P. K. Wong and C. Y. Jimmy, *Appl. Catal., B*, 2015, **176**, 444–453.
15 T. Jiang, K. Wang, T. Guo, X. Wu and G. Zhang, *Chin. J. Catal.*, 2020, **41**, 161–169.
16 Y. Qin, H. Li, J. Lu, C. Ma, X. Liu, M. Meng and Y. Yan, *Appl. Surf. Sci.*, 2019, **493**, 458–469.
17 C. Zhang, Y. Ma, C. Li, F. Qin, C. Hu, Q. Hu and S. Duo, *J. Mater. Sci.*, 2020, **55**, 3181–3194.
18 X. Dai, S. Yan, L. Cui and L. Shi, *Ceram. Int.*, 2020, **46**, 11261–11267.
19 Z. Wang, L. Jiang, K. Wang, Y. Li and G. Zhang, *J. Hazard. Mater.*, 2021, **410**, 124948.
20 S. Yu, Y. Zhang, M. Li, X. Du and H. Huang, *Appl. Surf. Sci.*, 2017, **391**, 491–498.
21 Z. Wang, K. Wang, Y. Li, L. Jiang and G. Zhang, *Appl. Surf. Sci.*, 2019, **498**, 143850.
22 C. Li, Y. Ma, S. Zheng, C. Hu, F. Qin, L. Wei, C. Zhang, S. Duo and Q. Hu, *J. Phys. Chem. Solids*, 2020, **140**, 109376.
23 J. Li, X. Wu, Z. Wan, H. Chen and G. Zhang, *Appl. Catal., B*, 2019, **243**, 667–677.
24 J. Li, Y. Li, G. Zhang, H. Huang and X. Wu, *ACS Appl. Mater. Interfaces*, 2019, **11**, 7112–7122.
25 D. Xia and I. M. Lo, *Water Res.*, 2016, **100**, 393–404.
26 D. A. Kozlov, V. Lebedev, A. Y. Polyakov, K. Khazova and A. V. Garshev, *Nanosyst.: Phys., Chem., Math.*, 2018, **9**, 266–278.
27 J. Wagner, T. Tshikhudo and J. Köhler, *Chem. Eng. J.*, 2008, **135**, S104–S109.
28 C. Wagner, W. Riggs, L. Davis, J. Moulder and G. Muilenberg, *Handbook of X-ray photoelectron spectroscopy*, Perking-Elmer Corporation, Physical Electronics Division, Eden Prairie, Minnesota, USA, 1979.
29 E. de Oliveira Jardim, S. Rico-Francés, F. Coloma, E. V. Ramos-Fernández, J. Silvestre-Albero and A. Sepúlveda-Escribano, *Appl. Catal., A*, 2014, **487**, 119–129.
30 D. H. Jung, Y. J. Oh, S. H. Lim, H. K. Kim and H. Lee, *J. Appl. Phys.*, 2021, **129**, 125301.
31 J. Wang, Z. Wang, B. Huang, Y. Ma, Y. Liu, X. Qin, X. Zhang and Y. Dai, *ACS Appl. Mater. Interfaces*, 2012, **4**, 4024–4030.
32 C. Deraedt, L. Salmon, S. Gatard, R. Ciganda, R. Hernandez, J. Ruiz and D. Astruc, *Chem. Commun.*, 2014, **50**, 14194–14196.
33 S. Tti, *Pure Appl. Chem.*, 1986, **58**, 955–966.
34 Y. Xu and M. A. Schoonen, *Am. Mineral.*, 2000, **85**, 543–556.